# Numerical simulation of the seakeeping of a military trimaran hull by a novel overset mesh method in regular and irregular waves

**Parviz Ghadimi[1]✉, Saeid Karami[2], Amin Nazemian[3]**

[1] https://orcid.org/0000-0002-9315-5428
[2] https://orcid.org/0000-0001-8959-3487
[3] https://orcid.org/0000-0001-6861-4488

[1,3] Amirkabir University of Technology, Department of Maritime Engineering
424 Hafez Ave, Tehran, Iran, e-mail: {pghadimi; anazemian}@aut.ac.ir
[2] Malek Ashtar University, Department of Maritime Engineering
Tehran, Iran, e-mail: s_karami_mut_ac@dr.com
✉ corresponding author

**Abstract**
The hydrodynamic performance of trimaran hulls has been previously investigated for optimum performance in calm water, but there is still a limited understanding of its motion response; therefore, a CFD-based numerical approach was developed and applied on a trimaran hull in the presence of regular and irregular waves. To validate the CFD method, a comparison was conducted using both experimental and 3D panel method data. In this study, two different turbulence models were surveyed, and the SST Menter k-Omega (k-ω) turbulence model was shown to be a more accurate model than the realizable k-Epsilon (k-ε) model. The different features of the proposed numerical model include the implementation of an overset mesh method, unique mesh plan refinement, and wave-damping region. The discrepancy between the experimental data and the results of other seakeeping calculation methods have always been problematic, especially for low-speed strip theory and 3D panel methods, but good consistency was observed between the proposed CFD model and experimental data. Unlike potential-based or conformal mapping seakeeping analysis methods, the effect of nonlinear waves, hull shape above the waterline, and other ship dynamic phenomena were considered in this CFD application. The proposed CFD method reduces the simulation time and computational efforts for ship motion calculations.

## Nomenclature

$A_w$ – wave amplitude (a.k.a. $\xi_0$ or $\xi_3$)
$a_0$ – vertical acceleration
$B$ – overall ship breadth
$C_T$ – total resistance coefficient
$C_\mu$ – realizable timescale coefficient (empirical)
$Fn$ – Froude number $= \sqrt{\dfrac{U}{gL_{pp}}}$

$g$ – gravitational acceleration
$H_w$ – wave height
$H_s$ – significant wave height
$k_{xx}$ – radii of gyration for roll motion
$k_{yy}$ – radii of gyration for pitch motion
$k_{zz}$ – radii of gyration for yaw motion
$k$ – turbulent kinetic energy
$k_w$ – wave number
$L_w$ – wavelength (a.k.a. $\lambda$)
$L_{pp}$ – length between perpendicular

$L_{wl}$ – length of waterline
$P$ – pressure
$q_\phi$ – forcing source term for wave absorbing
$r$ – refinement ratio
$R_T$ – total resistance
$T$ – viscous stress tensor
$T_w$ – wave period
$U$ – ship velocity
$u_i$ – fluid velocity
$\bar{u}_i$ – mean velocity
$u'_i$ – fluctuating velocity
$V$ – volume of cell
$V_i$ – volume of phase $i$
$x^*$ – wave forcing zone
$\alpha_i$ – volume fraction of phase $i$
$\gamma$ – forcing coefficient
$\mu_t$ – eddy viscosity
$\mu$ – kinematic viscosity
$\mu_s$ – vessel's moving direction
$\rho$ – fluid density
$\eta_3$ – heave motion
$\eta_4$ – roll motion
$\eta_5$ – pitch motion
$\varepsilon$ – turbulent dissipation rate
$\upsilon$ – kinematic viscosity
$\lambda_s$ – scale factor
$\omega_w$ – wave frequency
$\omega_e$ – encounter wave frequency
$\Delta$ – ship displacement

## Introduction

The hull form of a trimaran consists of a main hull and two side hulls, whose primary duty is to stabilize the ship. The unique features of this type of vessel are appropriate for general arrangements, especially their vast deck area, low resistance at high speed, and suitable resistance against damage. Despite extensive investigations into trimaran design concerning their resistance and components, limited research has been performed on seakeeping and real sea conditions. Most studies have concluded that the dynamic performance of these vessels is better than equivalent monohull vessels (Elcin, 2003; Ghadimi, Nazemian & Sheikholeslami, 2019; Gong et al., 2020). Most research has been conducted for resistance calculations and trimaran hull configurations that affect the flow characteristics around the hull (Xu & Zou, 2001; Sahoo & Lawrence, 2005; Slutski, 2008; Yanuar et al., 2013; Brizzolara et al., 2015; Akbari Vakilabadi et al., 2018; Nazemian & Ghadimi, 2020a). Hydrodynamic investigations in calm water are significantly different from wavy water surfaces.

Few studies have been devoted to seakeeping analyses of trimarans (Pastoor, Van't Veer & Harmsen, 2004; Fang & Too, 2006; Chou et al., 2008; Deng et al., 2019). The non-compliance between numerical and experimental results are problematic, especially for low-speed strip theory and 3D panel methods (Kurultay, 2003; Grafton, 2007; Dobashi, 2014). Due to the use of potential theory, most previous numerical approaches are limited in terms of considering the effect of viscosity and turbulence. Furthermore, traditional seakeeping analyses are limited to some constraints like linear theory, zero-speed conditions, wall-sided hulls, etc. (Bertorello et al., 2001; Yang et al., 2002; Doctors, 2015; Wang, Ma & Duan, 2018; Du, Hefazi & Sahoo, 2019; Li & Li, 2019).

CFD simulations of ship motion have been conducted in the past decade due to improvements in computer systems and CFD solvers. Simonsen et al. (Simonsen et al., 2013) performed a comprehensive CFD and EFD study on a KCS ship hull based on ship motion under different maritime conditions. Their research served as a benchmark study and uncertainty analyses for similar attempts. Wu et al. (Wu et al., 2011) studied a high-speed trimaran in regular head waves by using a CFD solver and compared their results with experimental data. Wu et al. proved the appropriate performance of the CFD tool by RANS equation solutions for seakeeping analyses.

CFD-based advanced studies have been developed in the past decade by some researchers. Hebblewhite et al. (Hebblewhite, Sahoo & Doctors, 2007) performed numerical and experimental investigations to determine the effects of the longitudinal position of the side hulls on the motions in the heave and pitch of a trimaran hull. Jia et al. (Jia, Zong & Shi, 2009) studied the resistance and seakeeping characteristics of a transom stern trimaran for different Froude numbers and sidehull arrangements. Tezdogan, Demirel, and Turan (Tezdogan, Demirel & Turan, 2014) used the RANS equation solver to study the seakeeping and operability of a commercial marine vessel. Another research of Tezdogan et al. (Tezdogan et al., 2014) illustrated that the RANS solver considers the effects of breaking waves, turbulence, and viscosity, which are not considered in the numerical simulations based on potential flow theories. Ghadimi et al. (Ghadimi, Nazemian & Ghadimi, 2019) investigated the sidehull arrangement of a wave-piercing trimaran in the presence of regular waves with different characteristics. They concluded that a lower stagger distance and higher clearance of the sidehull improved the seakeeping of a trimaran hull. Nowruzi et al. (Nowruzi et al., 2020) simulated

a trimaran hull using the CFD tool in different turbulence models and gridding configurations.

The surveyed literature shows that CFD solvers can predict the calm water resistance more accurately than other analytical or potential-based resistance calculation methods. Nevertheless, seakeeping performance assessments by CFD solvers require long computing times and effort, which are not suitable for comprehensive industrial investigations; thus, there is a lack of accurate and fast CFD approaches for the dynamics of marine vehicles. This paper has two main purposes. First, a low-cost and efficient CFD tool is developed for seakeeping analyses of marine vessels. Second, the response motion of a military trimaran hullform is surveyed in regular and irregular waves. To accomplish these tasks, a wave-piercing bow trimaran hull was simulated in the presence headsea waves by using a RANS equation solver (Star CCM+). Computations were validated and verified by available experimental data and Ansys AQWA solver. The experimental results of Akbari Vakilabadi et al. (Akbari Vakilabadi, Khedmati & Seif, 2014) and the 3D panel method were implemented to compare CFD calculations, and the main differences are discussed. A seakeeping study of a wave-piercing bow trimaran was implemented at different Froude numbers of 0.37 and 0.51 at different wavelengths. Ship motion was simulated by an overset mesh zone, which led to high-quality gridding around the hull. In addition, a VOF wave forcing method was applied to the numerical CFD model to create a damping zone to avoid the blockage effect and was extended to virtual towing tank boundaries, which reduced the number of meshes. Finally, a comparison of the obtained results illustrated the capability and superiority of the applied seakeeping analyses method for regular and irregular wave conditions.

## Problem definition

Due to the numerous maritime conditions for seagoing ships, the numerical analysis method should not be time-consuming in the design process. The selected methods must be both accurate and efficient. For example, simple seakeeping analyses for a ship consists of 240 runs (1).

Every run takes one day of CPU-time (see the presented example of relation (1)). Different maritime and sea environment conditions in seakeeping analyses lead to variations in ship operation modes. Two ship weight loading cases, two different ship speeds, two sea states and their corresponding wave

$$\frac{\text{ship weight}}{2} \cdot \frac{\text{speed (kn) }[16.30]}{2} \cdot$$
$$\cdot \frac{\text{wave height (m) }[4.6]}{2} \cdot$$
$$\cdot \frac{\text{heading (deg) }[180, 135, 90, 45, 0]}{5} \cdot$$
$$\cdot \frac{\text{wave length}[0.5L, 0.75L, 1L, 1.25L, 1.5L, 2L]}{6} = 240$$

(1)

heights, five heading angles, and six wavelengths are the seakeeping parameters used to construct a RAO plot; therefore, CFD analyses are not an efficient or acceptable method for seakeeping studies. In this regard, the present paper offers a numerical simulation that reduces the processing time without reducing accuracy. The present investigation includes a damping force method, gridding technique, and numerical parameters for the simulation, such as a turbulence model and time discretization methods. In this study, a model of wave-piercing bow trimaran ships is studied. The dimensional characteristics of this ship and model ($\lambda_s = 80$) are shown in Table 1. The ship has a wave-piercing bow, and the lateral bodies are made in the form of a Wigley hull that has been studied by Akbari Vakilabadi et al. (Akbari Vakilabadi, Khedmati & Seif, 2014). Figure 1 shows the 3D view of the trimaran model that was used in their tests. During rotation, radii of gyrations must be defined, which are presented in the last two rows of Table 1. $k_{xx}$ is the radius of gyration of roll motion and is defined to be equal to 0.444 $B$; $k_{yy}$ and $k_{zz}$ are the radius of gyration for the pitch and yaw motions, respectively, which are equal to 0.246 $L$; $L$ is the ship length; $B$ is the overall trimaran beam.

**Table 1. Specifications of the trimaran ship hull: the main vessel and the model type (Akbari Vakilabadi, Khedmati & Seif, 2014; Nazemian & Ghadimi, 2020b)**

| Specifications | Main vessel | Model |
|---|---|---|
| Overall length (m) | 124 | 1.55 |
| Draft length (m) | 123.2 | 1.54 |
| Total width (m) | 22.2 | 0.2722 |
| Main hull width (m) | 5 | 2.5 |
| Side hull length (m) | 36 | 0.45 |
| Draft (m) | 4.384 | 0.0548 |
| Clearance (side hull transverse distance) | 9.7 | 0.1212 |
| Stagger (side hull longitudinal distance) | 0 | 0 |
| Displacement | 2248.8 (Ton) | 4.39 (kg) |
| *x*-axis of the radii of gyration ratio ($k_{xx}/B$) | 0.444 | |
| *y*- and *z*-axis of the radii of gyration ratio ($k_{yy}/L$, $k_{zz}/L$) | 0.246 | |

**Figure 1. 3D view of the studied trimaran ship**

**Numerical scheme**

Utilizing the Reynolds-Averaged Navier-Stokes (RANS) equation solver, seakeeping simulations were performed by StarCCM+ software. Furthermore, two different turbulent models are surveyed: the realizable k-ε and the SST Menter k-ω approach. The physical model was selected based on the StarCCM+ user guide (User Guide, 2020) and ITTC recommendations (ITTC Recommendations, 2011; 2014). The unsteady scheme with a physical time step of 0.01 s was used for temporal discretization, and the SIMPLE algorithm was applied for coupling the pressure and velocity equations. The governing equations of continuity in equation (2) and momentum conservation in equation (3) for the three-dimensional incompressible flow are expressed as follows:

$$\frac{\partial u_i}{\partial x_i} = 0 \qquad (2)$$

$$\frac{\partial u_i}{\partial t} + \frac{\partial}{\partial x_i}\left(u_i u_j\right) =$$

$$= -\frac{1}{\rho}\frac{\partial p}{\partial x_i} + \mu \frac{\partial}{\partial x_j}\left(\frac{\partial u_i}{\partial x_j} + \frac{\partial u_j}{\partial x_i}\right) + \frac{\partial}{\partial x_j}\left(-\overline{u_i' u_j'}\right) \quad (3)$$

The mean pressure is represented by $p$, the fluid density $\rho$, and the kinematic viscosity of the fluid $\mu$, where the velocity $u_i$ can be decomposed into the mean velocity $\bar{u}_i$ and fluctuating velocity $u'_i$, which is expressed by equation (4):

$$u_i = \bar{u}_i + u_i' \qquad (4)$$

The Reynolds stress tensor that appears in the momentum transport equation is calculated by:

$$\overline{u_i' u_j'} = -\mu_t\left(\frac{\partial u_i}{\partial x_j} + \frac{\partial u_j}{\partial x_i}\right) + \frac{2}{3}\delta_{ij}k \qquad (5)$$

where $\mu_t$ is the eddy viscosity, which can be calculated by different methods. Two basic turbulence models, realizable k-ε and SST K-Omega approaches are applied herein. The turbulent viscosity ($\mu_t$) for realizable k-ε and SST K-Omega turbulence models was calculated using equations (6) and (7), respectively:

$$\mu_t = C_\mu \frac{k^2}{\varepsilon} \qquad (6)$$

$$\mu_t = kT \qquad (7)$$

where $C_\mu$ is a realizable time scale coefficient; $k$ is the turbulent kinetic energy; $\varepsilon$ is the turbulent dissipation rate; $T$ is the viscous stress tensor. The volume of fluid method was applied to capture the free surface of water. The fields of the phase volume fraction describe the distribution of phases and the interface position $\alpha_i$. The volume fraction of phase $i$ is defined as:

$$\alpha_i = \frac{V_i}{V} \qquad (8)$$

where $V$ is the volume of a cell, and $V_i$ is the volume of phase $i$ in the cell. The volume factions of all phases in this cell are satisfied with equation (9):

$$\sum_{i=1}^{N} \alpha_i = 1 \qquad (9)$$

where $N$ is the total number of phases. Since there are two phases (water and air), $N = 2$.

Two regular and irregular waves were applied in the seakeeping analyses by defining VOF waves. In the surrounding boundaries, a wave force function was added to the fluid transport (momentum) equations. The forcing source terms adapted the solution to the simplified solution that was imposed at the reduced domain boundary. This forcing term resolves wave reflection problems at the boundaries (Kim, O'Sullivan & Read, 2012; Kim et al., 2019; User Guide, 2020). This source term is defined by equation (10):

$$q_\phi = -\gamma\rho\left(\phi - \phi^*\right) \qquad (10)$$

where $\gamma$ is the forcing coefficient, which is expressed by equation (11); $\rho$ is the fluid density; $\phi$ is the current solution of the momentum equation; $\phi^*$ the value regarding the forced solution. The defined forcing zone and its distance are displayed in Figure 2. The forcing source term was not applied within the inner zone (3D Navier-Stokes), but within the outer zone (Forcing zone), the forcing source term was activated along the solution domain boundaries. The forcing coefficient ($\gamma$) varied smoothly from zero at the inner edge of the forcing zone ($x^*$) to the maximum value at the boundary (the outer edge of the forcing zone) (Kim et al., 2019; User Guide, 2020).

$$\gamma = -\gamma_0 \cos^2\left(\frac{\pi x^*}{2}\right) \qquad (11)$$

The inner and outer edges of the damping zone are respectively represented by $x_{sd}$ and $x_{ed}$. Accordingly, $\cos^2$ is defined by:

$$\frac{\pi x^*}{2} = \frac{\pi}{2} + \frac{\pi}{2} \frac{x - x_{sd}}{x_{ed} - x_{sd}} \Rightarrow \text{herein}: x^* = \frac{x}{1.5} \quad (12)$$

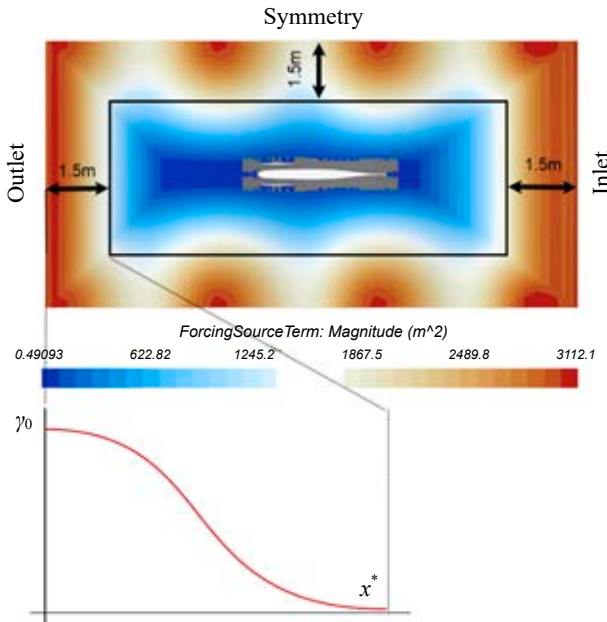The damping zone and forcing coefficient variation are depicted in Figure 2 by a contour and damping intensity plot.



**Figure 2. Wave forcing zone and boundary length distance (1.5 m) for the surrounding boundaries**

Simulations were conducted by the dynamic fluid body interaction (DFBI) module in order to calculate the ship motions. The ship could freely move with 2 degrees of freedom of heave and pitch motions. The simulation domain and the name of its boundaries are shown in Figure 3. The inlet boundary defines the velocity inlet boundary condition and was located 1.5 $L$ in front of the forward perpendicular. The top and bottom of the domain are defined as the inlet velocity and are located 1 $L$ and 1.5 $L$ from the trimaran's C.G., respectively. The pressure outlet boundary condition was applied at the outlet boundary, which extended 1.5 $L$ from the aft perpendicular. The width of the virtual tank is 1 $L$, and the symmetry plane was defined for the side and symmetry boundaries of the computational domain. All of the defined distance and ship hull locations are displayed in Figure 4.

**Mesh study**

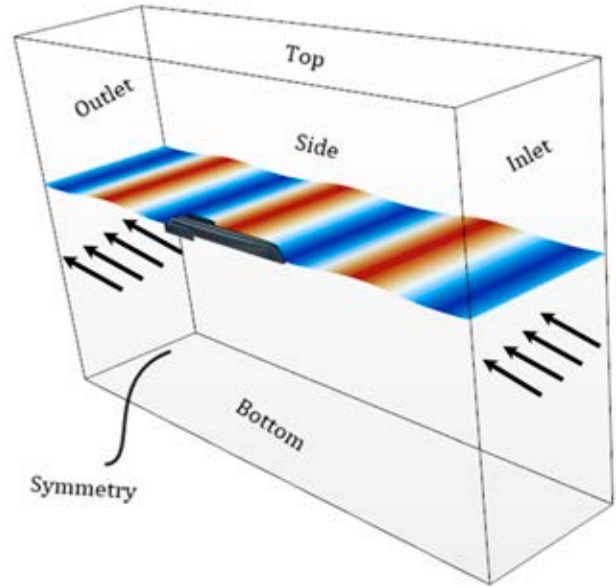An unstructured trimmer mesh was adopted for mesh operations following the ITTC recommenda-



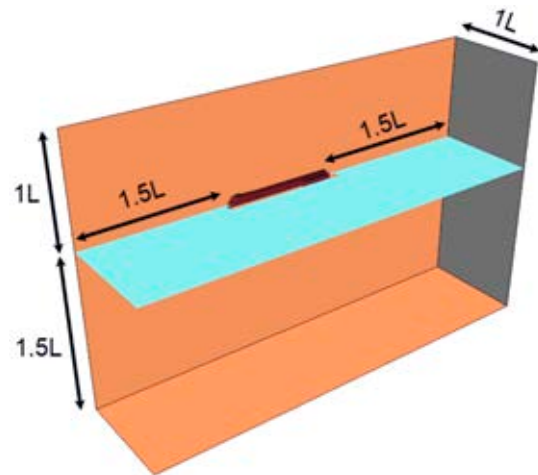**Figure 3. Computational domain and domain boundaries**



**Figure 4. Trimaran ship location of the virtual tank and its boundaries**

tions (ITTC Recommendations, 2011; 2014) and Star CCM+ user guide (User Guide, 2020). To capture waves acting on the free surfaces and sharp corners of the hull, surface and volumetric refinements were applied to the volume mesh. 25% of the base size mesh refinement was applied for the $x$-direction and 12.5% anisotropic mesh size was finer in the $z$-direction. $x$-direction and $z$-direction mesh refinement was performed to capture the wavelength and wave height around the free surfaces. Figure 5 illustrates the selected mesh characteristics. A mesh study was implemented to select the appropriate base size of the mesh cell. Mesh refining and grid convergence was continued until the solutions became independent of the mesh size.

The wave elevation on a free surface is a control variable for mesh convergence. The initial mesh
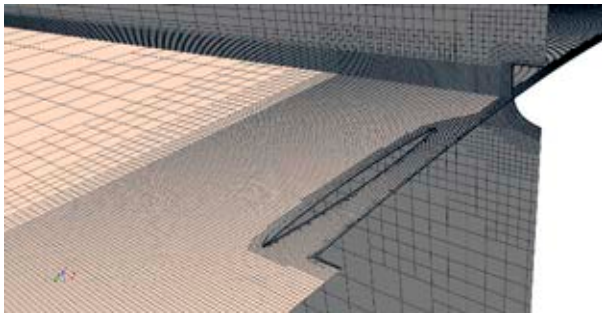
**Figure 5. Domain and overset region gridding**

size adopted in this investigation was $L_w/60$; four mesh plans were made according to the refinement ratio of $\sqrt[3]{2}$. A regular linear wave was adopted for mesh plan validation. The wave characteristics are described in Table 2, where $T_w$ is the wave period, $H_w$ is the wave height, $L_w$ is the wavelength, $k_w$ is the wave number, and $A_w$ is the wave amplitude. In addition, the specific parameters of the mesh plans are shown in Table 3.

**Table 2. Regular wave characteristics**

| $T_w$ (s) | $k_w$ | $L_w$ (m) | $H_w$ (m) | $A_w$ (m) |
|---|---|---|---|---|
| 1.07 | 3.5 | 1.8 | 0.05 | 0.025 |

**Table 3. Mesh plan parameters and sizes**

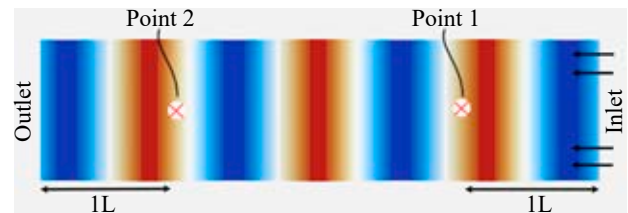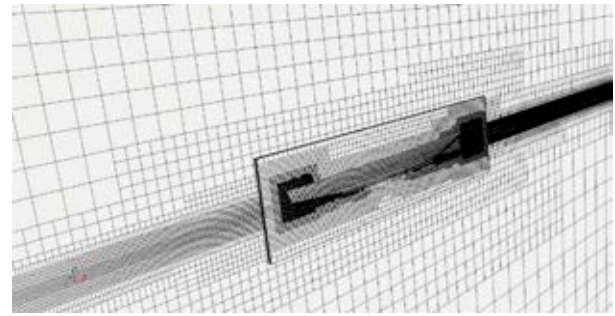| Mesh | Base size | Number of cells per wavelength | Number of cells per wave height | Total number |
|---|---|---|---|---|
| Grid1 | 0.125 | 60 | 12 | 725,340 |
| Grid2 | 0.085 | 80 | 16 | 1,004,395 |
| Grid3 | 0.06 | 105 | 20 | 1,358,273 |
| Grid4 | 0.042 | 134 | 25 | 1,788,094 |



**Figure 6. Two history probe points for surface elevation recording**

Two history probe points were located 1 $L$ from the inlet and outlet boundaries to record the wave elevation (Figure 6). The wave elevations at different grid plans for points 1 and 2 are shown in Figure 7a and Figure 7b, respectively. When the waves reached point 2, the wave amplitudes were reduced by about 4% compared to Point 1 due to physical and numerical dissipation. The differences in the wave elevation between the incident wave height and the measured wave height at point 2 calculated by these four types of meshes were 3.44%, 2.86%, 1.95%, and 1.52%, from grid 1 to grid 4. Considering the accuracy and computational costs, grid 3 was selected as the optimum mesh plan.
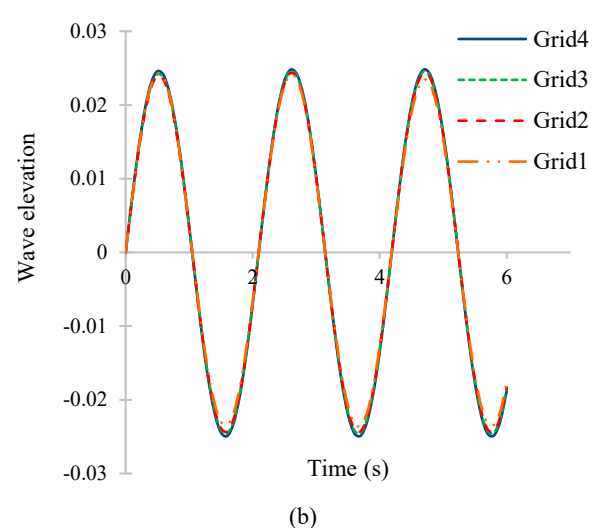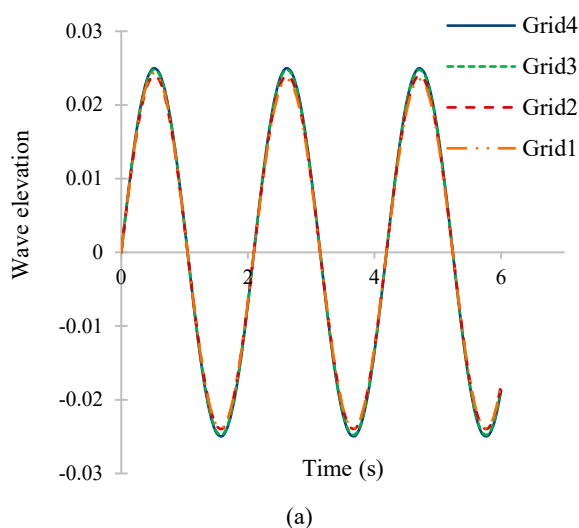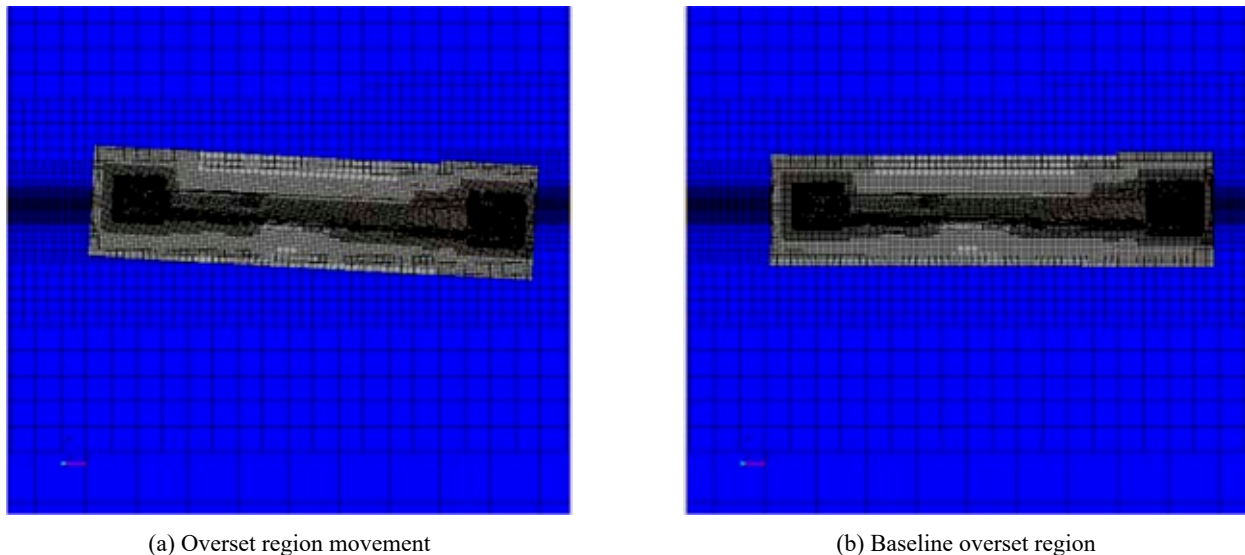


**Figure 7. Wave elevation at (a) Point 1 near the inlet boundary and (b) Point 2 near the outlet boundary**

(a) Overset region movement



(b) Baseline overset region

**Figure 8. The defined overset mesh regions**

**Overset mesh**

An overset mesh region was developed in the computational domain. A high-resolution mesh configuration near the ship hull and free surface were adopted based on an overset mesh set-up (Simonsen et al., 2013; Nowruzi et al., 2020). The trimaran hull body includes an overset region. The overset mesh region moves with the hull (moving mesh) over a fixed background mesh of the domain. The overset mesh implementation reduces the computational time and generates a refined mesh system without compromising the accuracy. The overset mesh regions for the present numerical simulations are shown in Figure 8. In Figure 8a, the region translates and rotates at the end of the run. Accordingly, Figure 8b displays the initial position of the overset mesh region.

**Validation and verification**

A comparative study was implemented in two different turbulent models. The k-ω and k-ε models are similar to each other when solving two transport equations, but they are different in the choice of the second transported turbulence variable. The realizable k-ε model defines a new transport equation for the turbulent dissipation rate ε. The realizable two-layer k-ε model combines the model with a two-layer approach (Nowruzi et al., 2020; User Guide, 2020). The k-ω turbulence model is a two-equation model that solves transport equations for the turbulent kinetic energy $k$ and the specific dissipation rate $\omega$ – the dissipation rate per unit turbulent kinetic energy ($\omega = \varepsilon/k$) – in order to determine the turbulent eddy

viscosity. Menter's SST (shear-stress transport) k-ω model uses the insensitivity to free-stream conditions of the k-ε model in the far-field while retaining the advantages of the k-ω model near walls.

The two turbulence models mentioned above were utilized to examine their effectiveness in this study. In Figure 9, the motions are plotted against the physical time in headsea waves with a 0.025 m amplitude and wavelength of 1.8 m and a ship model speed of 1.44 m/s.

The comparison illustrates that both turbulent methods are suitable for seakeeping analyses, and the values of the SST k-ω turbulent method are closer than the k-ε method to experimental results. So, the SST k-ω turbulent method was selected for the following simulations.

**Seakeeping analyses**

A seakeeping study was carried out in regular and irregular waves under headsea conditions. The velocity of the ship model was $U$ = 1.44 m/s, corresponding to a Froude number of 0.37. The coordinate system was located on the vessel's center of gravity, and it moves along the x-direction. Figure 10 illustrates the coordinate system and the defined directions of irregular waves. The outputs of the CFD simulations are represented by the response amplitude operator (RAO), and the 3D panel method results were acquired by Ansys AQWA software. To extract statistical parameter values, the moment of the spectrum was calculated. Thus, the wave spectrum was multiplied by the square of the RAOs to obtain the response spectrum. RAO is defined by (Bhattacharyya, 1978):
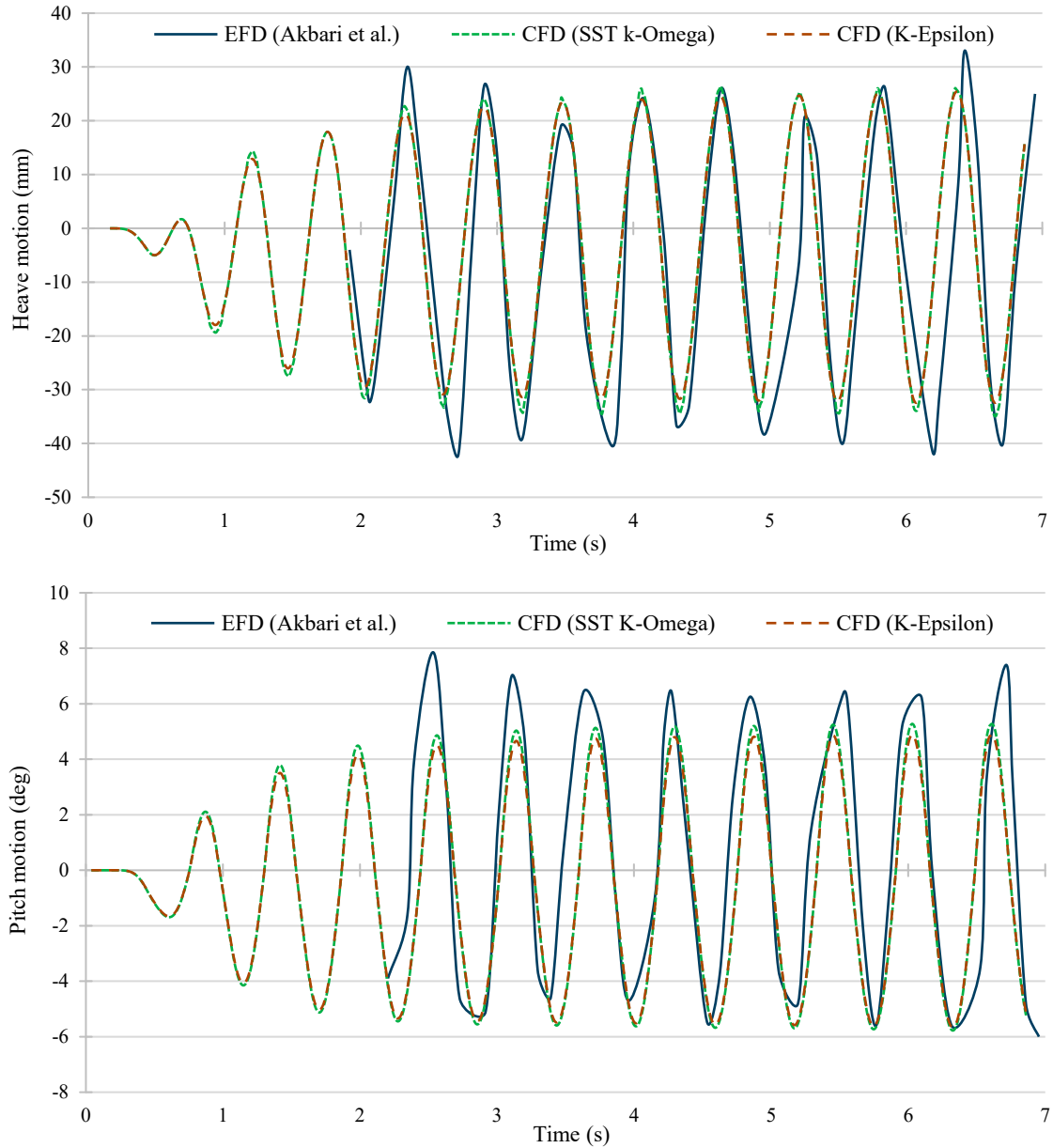
**Figure 9. Two turbulence model results and experimental verification for heave and pitch motion in a ship model speed of 1.44 m/s, wave amplitude of 0.025 mm, and wavelength of 1.8 m**

$$\text{Heave RAO} = \text{RAO}_3 = \frac{\eta_3}{\xi_0}$$

$$\text{Pitch RAO} = \text{RAO}_5 = \frac{\eta_5}{k\xi_0}$$

$$\text{Vertical acceleration} = \text{RAO}_a = \frac{a_0}{\omega_e^2 \xi_0} \quad (13)$$

$$S_x(\omega_e) = (\text{RAO}_x(\omega_e))^2 S_{\xi_0}(\omega_e), \quad x = 3.5 \quad (14)$$

The parameters $\eta_3$ and $\eta_5$ represent the heave and pitch motion values, respectively; $a_0$ is vertical acceleration; $\xi_0$ represents the wave amplitude (also shown as $\xi_3$); $k$ is the wave number, which is used to non-dimensionalize the motions. In order to obtain the encounter spectrum $S_{\xi_0}(\omega_e)$ of the vessel from the sea spectrum $S_{\xi_0}(\omega_w)$ and change the wave frequency ($\omega_w$) to the encounter frequency ($\omega_e$), the following equations are used:

$$\omega_e = \omega_w - \frac{\omega_w^2}{g} U \cos\mu_s \quad (15)$$

$$S_{\xi_0}(\omega_e) = S_{\xi_0}(\omega_w) \frac{1}{1 - \frac{2\omega_w U}{g} \cos\mu_s} \quad (16)$$

The vessel's moving direction ($\mu_s$) is 180°. Finally, the significant amplitude of motion and acceleration was calculated by the zeroth moment of the response spectrum.

$$\text{Significant value} = 2\sqrt{m_0} \quad (17)$$

$$m_n = \int_0^\infty \omega_e^n S_x(\omega_e)d\omega_e \Rightarrow m_0 = \int_0^\infty S_x(\omega_e)d\omega_e \quad (18)$$



**Figure 10. Irregular wave and coordinate system of seakeeping analyses**

The experimental results of Akbari Vakilabadi et al. (Akbari Vakilabadi, Khedmati & Seif, 2014) were taken into consideration as an EFD comparison. They tested different wavelength-to-ship length ratios ($\lambda/L$) for an under-studied trimaran hull.

## Results and discussion

### Regular wave computations

The obtained results of the proposed numerical model are compared against experimental data and 3D panel method responses. All results pertain to the seakeeping behavior under headsea conditions and regular waves with an amplitude of 0.025 m. Figures 11 and 12 illustrate the comparison of the obtained RAO values for the vessel's heave motions at two different Froude numbers of 0.37 and 0.51, respectively. Figures 13 and 14 display the RAO values of the pitch motions for the mentioned ship speeds. Parameters $\eta_3$, $\eta_4$, and $\eta_5$ represent the heave, roll, and pitch motion values, respectively. $\xi_3$ represents the wave amplitude, and $k$ is the wave number that is used to non-dimensionalize the motions. All of the obtained results are expressed for 6 different wavelengths, which include the horizontal axis of the graphs with a dimensionless ratio ($\lambda/L$). The CFD results are more consistent with the experimental results; however, the pitch motion results show a slight difference between the CFD and experimental results at $Fn = 0.51$. Based on the presented
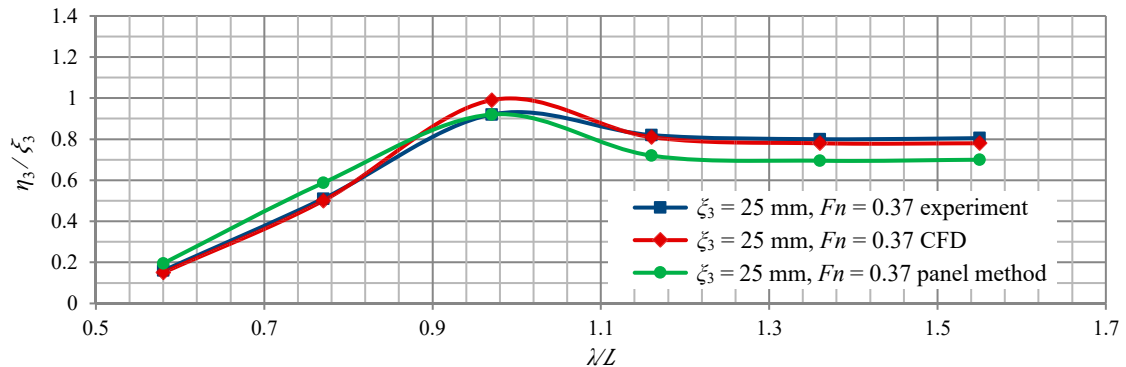


**Figure 11. Heave RAO as a function of non-dimensional encountering wavelengths for the trimaran at a Froude number of 0.37 and a wave amplitude of 25 mm**
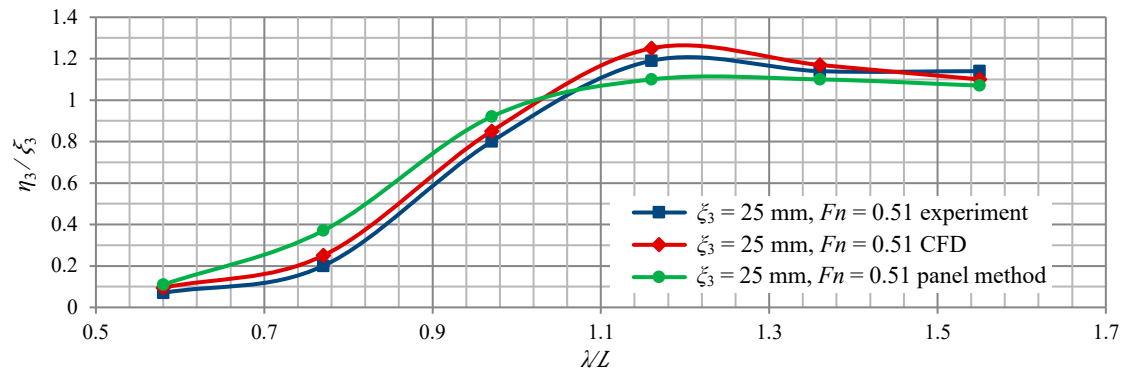


**Figure 12. Heave RAO as a function of non-dimensional encountering wavelength for the trimaran at a Froude number of 0.51 and a wave amplitude of 25 mm**
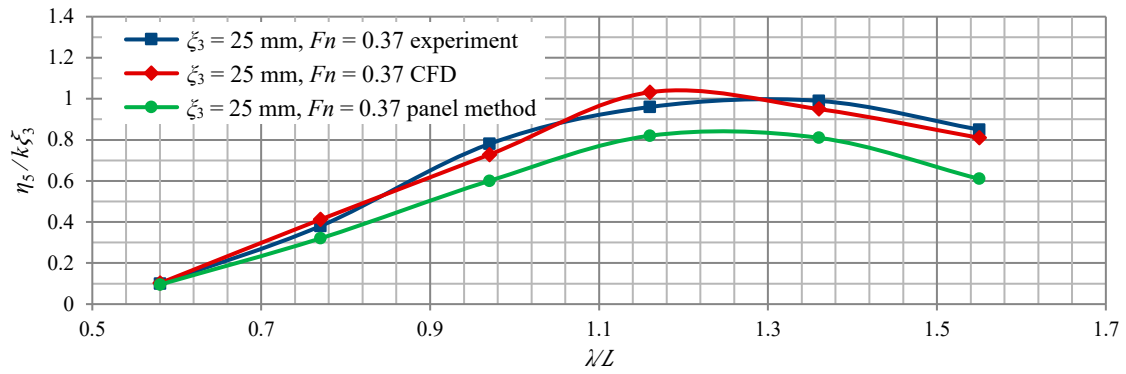
**Figure 13. Pitch RAO as a function of non-dimensional encountering wavelength for the trimaran at a Froude number of 0.37 and wave amplitude of 25 mm**
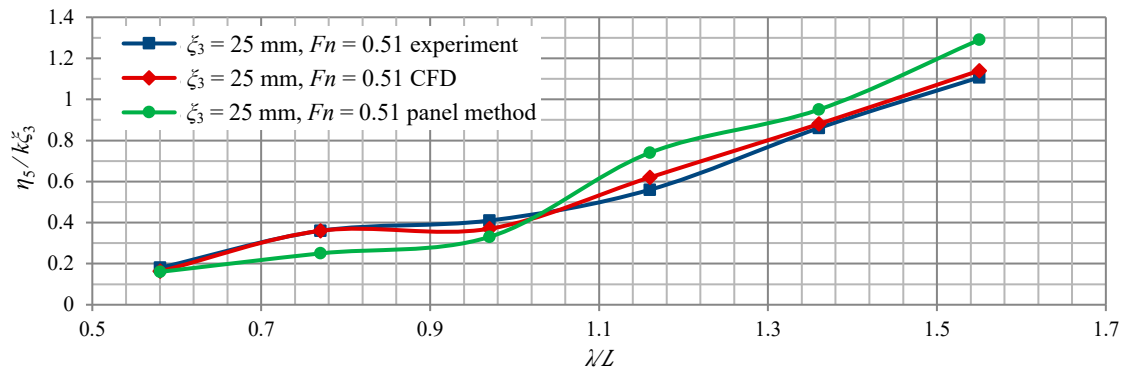


**Figure 14. Heave RAO as a function of non-dimensional encountering wavelength for the trimaran at a Froude number of 0.37 and wave amplitude of 25 mm**

comparisons, one may conclude that the proposed numerical model can accurately model motion characteristics. There is a significant difference between the 3D panel method results and the CFD and EFD data, especially the pitch motion at both speeds. This inconsistency was due to linearity assumptions and neglecting the effect of variations in the hullform above and below the waterline.

As observed in Figures 11 and 12, the heave motion of the trimaran does not change at high wavelength values. The RAO of the heave motion

illustrates that the magnitude of the heave amplitudes was equal to the wave amplitudes at a higher $\lambda/L$. In heave motions at different Froude numbers and different pitch motions at $Fn = 0.37$, a resonance peak was observed. Besides, the pitch motion at higher speeds and higher wavelengths yielded rough motion conditions, which caused offensive dynamic phenomena to occur. CFD simulation results were similar to the experiment data at most wavelengths; however, in some cases, the calculated motion response was slightly higher than the measured
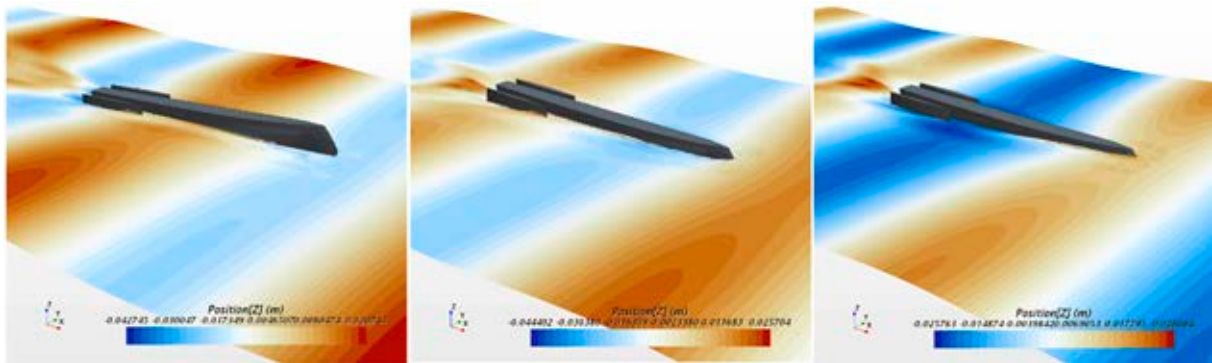


**Figure 15. Ship motion at different time steps (i.e., slamming phenomena)**
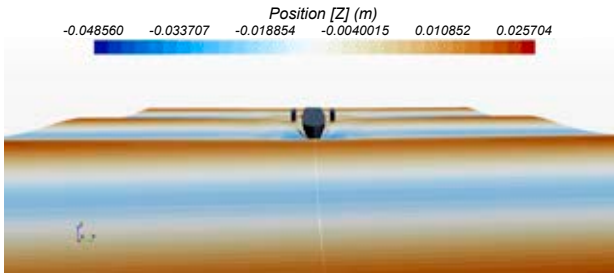
**Figure 16. Front view of the ship motion in the presence of a regular wave**

experimental value. This seemed to primarily happen at the resonance condition. A possible source of discrepancy may be the wave dissipation among the virtual tank.

Figure 15 shows the ship's motion at different time steps, which shows that regular headsea waves caused slamming phenomena. The forefoot region of the trimaran emerged from the water and then returned to the sea at a high vertical speed. The front view of the ship motion is depicted in Figure 16.
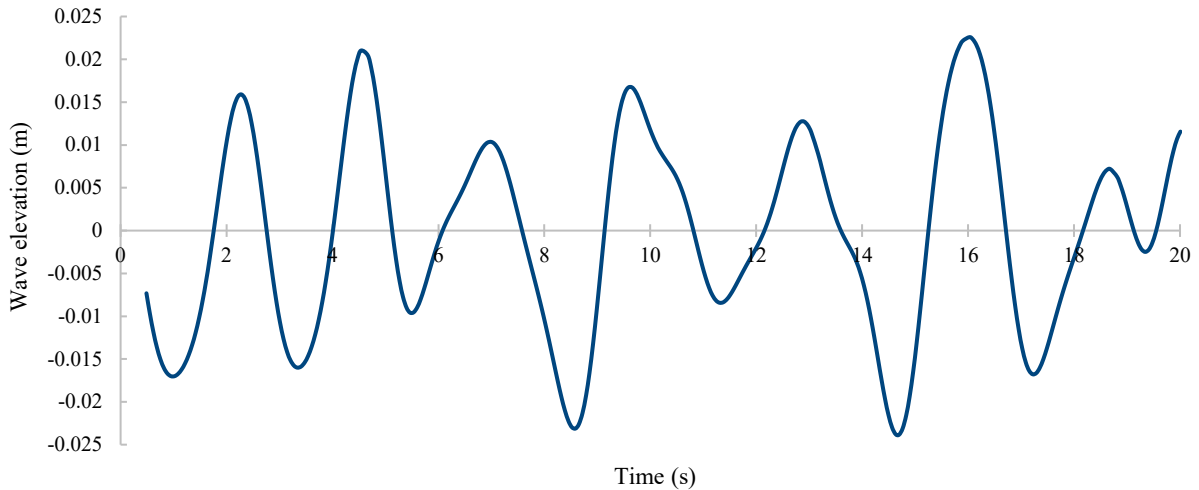


**Figure 17. Time history of recorded irregular waves Pierson-Moscowitz spectrum under the headsea condition of *Hs*=0.05 m**
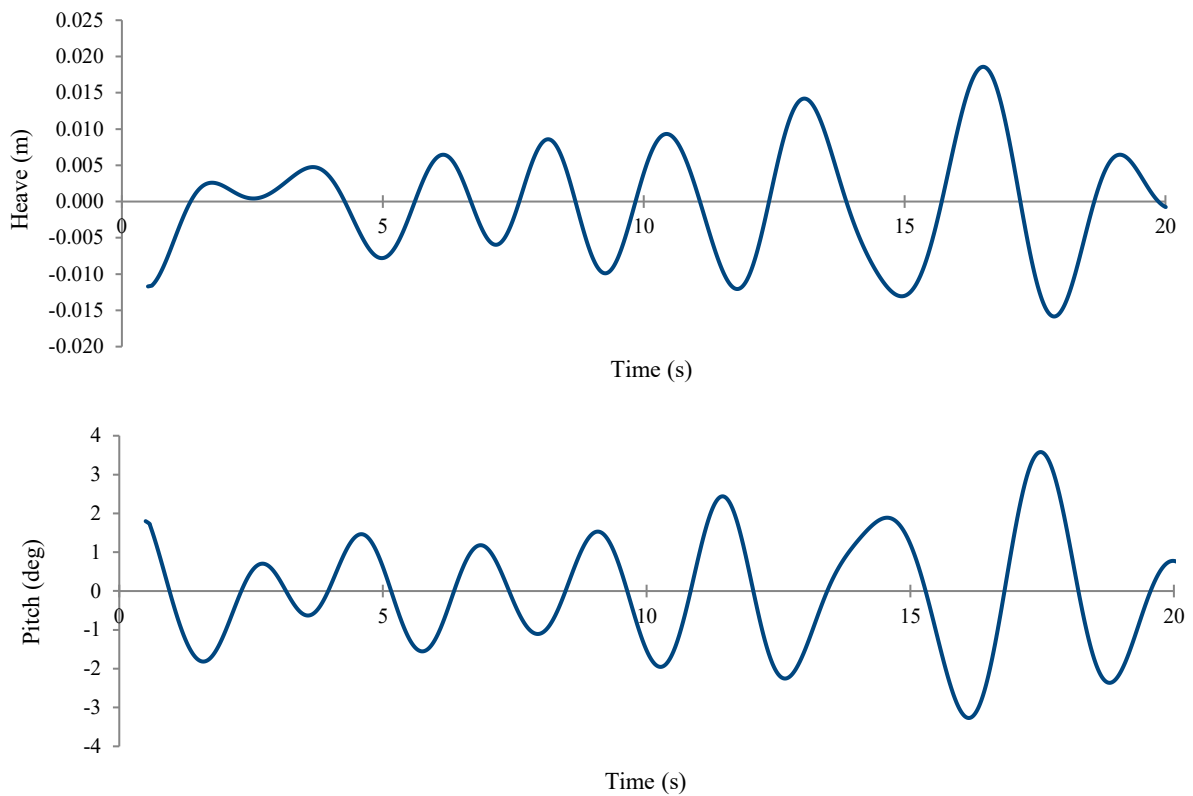




**Figure 18. Heave and pitch motion waves encountered at 180° at a Froude number of 0.37**

### Irregular wave computations

In this section, a seakeeping simulation was carried out in the presence of irregular Pierson-Moscowitz spectrum waves. The significant wave height was considered to be 0.05 m and the modal period was 1.07 s. The ship velocity was 1.44 m/s (for the model) with a headsea. Figure 17 displays the time history of the recorded irregular waves over 20 s, and Figure 18 shows the heave and pitch motions of the hull in irregular time-domain waves.

The performance of the CFD model can be observed in the results. The viscosity effects, nonlinear phenomena, and complex hull bodies are challenges in seakeeping studies that can be analyzed by CFD simulations. Besides, the complicated ship motion in irregular waves can be simulated by considering real sea conditions. The present seakeeping study can be developed for other maritime projects.

### Conclusions

Developing a more accurate and efficient numerical tool for seakeeping analyses of marine vessels was the basic aim of this paper. Accordingly, a CFD model for calculating the ship response in regular and irregular head sea waves was established. Two important techniques were used to accomplish this task. An overset mesh technique was implemented to simulate the vessel motion, and a wave forcing equation was applied to create a damping zone around the domain. The wave forcing term was executed in the damping region far from the hull, which reduced the domain size and number of meshes. The CFD results were consistent with the experimental data, as shown by the comparison of the time history for two different turbulent models and RAO plots for heave and pitch motions. Furthermore, two different turbulence models were investigated, and the SST Menter k-ω turbulence model was more accurate than the realizable k-ε model. A comparison of the proposed CFD model and 3D panel method with experimental results illustrated the accuracy and superiority of the present model for different maritime conditions. These comparisons were carried out at two different Froude numbers. The calculated pitch motion data in the 3D panel method was less consistent with the experimental results; however, in both heave and pitch motions, the CFD results showed compliance with the experiment data. In some cases, the CFD calculated motion response was slightly higher than the measured experimental values. A possible source of discrepancy may be the wave dissipation among the virtual tank, especially under resonance. Unlike traditional seakeeping analysis methods, the effect of nonlinear waves, hull shape above the waterline, and other ship dynamic phenomena were considered in the CFD applications. The presented CFD method reduces the simulation time and computational efforts for ship motion analyses. The proposed CFD tool may be useful for marine and maritime industrial applications for seakeeping studies.

### Acknowledgment

### References

1. Akbari Vikilabadi, K., Khedmati, M.R., Hasanabadi, A. & Mohammadi, A. (2018) Resistance Prediction for a Novel Trimaran with Wave Piercing Bow. *International Journal of Maritime Technology* 9, pp. 33–40.
2. Akbari Vikilabadi, K., Khedmati, M.R. & Seif, M.S. (2014) Experimental study on heave and pitch motion characteristics of a wave-piercing trimaran. *Transactions of Famena* 38(3), pp. 13–26.
3. Bertorello, C., Bruzzone, D., Cassella, P. & Zotti, I. (2001) Trimaran Model Test Results and Comparison with Different High-Speed Craft. In: *Practical Design of Ships and Other Floating Structures* 1, pp. 143–149.
4. Bhattacharyya, R. (1978) *Dynamics of marine vehicles*. U.S. Naval Academy.
5. Brizzolara, S., Vernengo, G., Pasquinucci, C. & Harries, S. (2015) *Significance of parametric hull form definition on hydrodynamic performance optimization*. In: 6th International Conference on Computation Methods in Marine Engineering (Marine 2015), pp. 254–265.
6. Chou, SK., Wu, H.T., Wu, C.H. & Hwang, J.L. (2008) *Investigation on seakeeping performance of the high-speed trimaran*. Proceedings of the 8th National Congress on Hydrodynamics, Ji-nan, China.
7. Deng, R., Luo, F., Wu, T., Chen, S. & Li, Y. (2019) Time-domain numerical research of the hydrodynamic characteristics of a trimaran in calm water and regular waves. *Ocean Engineering* 194, 106669.
8. Dobashi, J. (2014) On the prediction method for ship motions of trimaran in oblique waves. *Journal of the Japan Society of Naval Architects and Ocean Engineers* 20, pp. 77–84.
9. Doctors, L.J. (2015) *Hydrodynamics of high-performance marine vessels*. Charleston, SC: CreateSpace Independent Publishing Platform.
10. Du, L., Hefazi, H. & Sahoo, P. (2019) Rapid resistance estimation method of non-Wigley trimarans. *Ships and Offshore Structures* 14(2), pp. 1–11.
11. Elcin, Z. (2003) *Wave making resistance characteristics of trimaran hulls*. Master's Thesis, Naval Postgraduate School, Monterey, California. Available from: https://apps.dtic.mil/sti/pdfs/ADA420575.pdf [Accessed: October 10, 2020].

12. FANG, M.C. & TOO, G.Y. (2006) The Effect of Side Hull Arrangements on the Motions of the Trimaran Ship in Waves. *Naval Engineering Journal* 118(1), pp. 27–37.

13. GHADIMI, P., NAZEMIAN, A. & GHADIMI, A. (2019) Numerical scrutiny of the influence of side hulls arrangement on the motion of a Trimaran vessel in regular waves through CFD analysis. *Journal of the Brazilian Society of Mechanical Science and Engineering* 41, 1.

14. GHADIMI, P., NAZEMIAN, A. & SHEIKHOLESLAMI, M. (2019) *Numerical simulation of the slamming phenomenon of a wave-piercing trimaran in the presence of irregular waves under various seagoing modes.* Proceedings of the Institution of Mechanical Engineers, Part M: Journal of Engineering for the Maritime Environment 233(4), pp. 1198–1211.

15. GONG, J., YAN, S., MA, Q. & LI Y. (2020) Added resistance and seakeeping performance of trimarans in oblique waves. *Ocean Engineering* 216, 107721.

16. GRAFTON, T.J. (2007) *The roll motion of trimaran ships.* Doctor's of Philosophy Thesis, University College London. Available from: https://discovery.ucl.ac.uk/id/eprint/1445979/2/Grafton_vol2edit.pdf. [Accessed: October 10, 2020].

17. HEBBLEWHITE, K., SAHOO, P.K. & DOCTORS, L. (2007) A case study: theoretical and experimental analysis of motion characteristics of a trimaran hull form. *Ships and Offshore Structures* 2, pp. 149–156.

18. ITTC Recommendations (2011) ITTC-Recommended Procedures and Guidelines, Practical Guidelines for Ship CFD Applications, 7.5-03-02-03.

19. ITTC Recommendations (2014) ITTC-Recommended Procedures and Guidelines, Practical Guidelines for Ship Resistance CFD, 7.5-03-02-04.

20. JIA, JB., ZONG, Z. & SHI, H.Q. (2009) Model experiments of a trimaran with transom stern. *International Shipbuilding Progress* 56(3), pp. 119–133.

21. KIM, J.W., O'SULLIVAN, J. & READ, A. (2012) *Ringing Analysis on a Vertical Cylinder by Euler Overlay Method.* 31st International Conference on Ocean, Offshore and Arctic Engineering, paper No. OMAE2012-84091, pp. 855–866, Rio de Janeiro, Brasil.

22. KIM, Y., PARK, C., KIM, J., LEE, H. & JIN, I. (2019) Numerical simulations of added resistance in regular head waves on a container ship. *Brodogradnja* 70(2), pp. 61–86.

23. KURULTAY, A.A. (2003) *Sensitivity analysis of the seakeeping behaviour of trimaran ships.* Master's Thesis, Naval Postgraduate School, Monterey, California (USA).

24. LI, A. & LI, Y. (2019) Numerical and experimental study of seakeeping performance of a high-speed trimaran with T-foil. *Polish Maritime Research* 26(3), pp. 65–77.

25. NAZEMIAN, A. & GHADIMI, P. (2020a) Shape optimisation of trimaran ship hull using CFD-based simulation and adjoint solver. *Ships and Offshore Structures* October 2020, pp. 1–15.

26. NAZEMIAN, A. & GHADIMI, P. (2020b) *Multi-objective optimization of trimaran sidehull arrangement via surrogate-based approach for reducing resistance and improving the seakeeping performance.* Proceedings of the Institution of Mechanical Engineers, Part M: Journal of Engineering for the Maritime Environment. December 2020:1475090220980275.

27. NOWRUZI, L., ENSHAEI, H., LAVROFF, J., KIANEJAD, S.S. & DAVIS M.R. (2020) CFD Simulation of Motion Response of a Trimaran in Regular Head Waves. *International Journal of Maritime Engineering* 162(A1), pp. 91–106.

28. PASTOOR, W., VAN'T VEER, R. & HARMSEN E. (2004) *Seakeeping behaviour of a frigate-type trimaran.* Proceedings of the International Conference on the Design and Operation of Trimaran Ships, Royal Institute of Naval Architects (RINA), 29–30 April, London (U.K.).

29. SAHOO, P.K. & LAWRENCE, J. (2005) *The waves generated by a trimaran.* Proceedings of the 8th International Conference on the Fast Sea Transportatioin, Saint Petersburg, Russia.

30. SIMONSEN, C.D., OTZEN, J.F., JONCQUEZ, S. & STERN, F. (2013) EFD and CFD for KCS heaving and pitching in regular head waves. *Journal of Marine Science and Technology* 18, pp. 435–459.

31. SLUTSKI, J. (2008) Resistance and component hull interactions of a high-speed trimaran sealift ship. NSWCCD, 50-TR-2008/093.

32. TEZDOGAN, T., DEMIREL, Y. K., INCECIK, A. & TURAN, O. (2014) *Hydrodynamics of heaving twin cylinders in a free surface using an unsteady-RANS method.* The 2nd International Conference on Maritime Technology (ICMT2014).

33. TEZDOGAN, T., DEMIREL, Y.K. & TURAN, O. (2014) Operability assessment of high-speed passenger ships based on human comfort criteria. *Ocean Engineering* 89, pp. 32–52.

34. User Guide (2020) StarCCM+ version 2020.1. SIEMENS Simcenter.

35. WANG, S., MA, S. & DUAN, W. (2018) Seakeeping optimization of trimaran outrigger layout based on NSGA-II. *Applied Ocean Research* 78, pp. 110–122.

36. WU, C., ZHOU, D., GAO, L. & MIAO, Q. (2011) CFD computation of ship motions and added resistance for a high-speed trimaran in regular head waves. *International Journal of Naval Architecture and Ocean Engineering* 3(1), pp. 105–110.

37. XU, H. & ZOU, Z. (2001) *Numerical prediction of wave-making resistance of a trimaran.* Proceedings of 2nd International Workshop on Ship Hydrodynamics (IWSH'01), Wuhan, China, pp. 105–109.

38. YANG, C., SOTO, O., LÖHNER, R. & NOBLESSE, F. (2002) Hydrodynamic optimization of a trimaran. *Ship Technology Research* 49(2), pp. 70–92.

39. YANUAR, Y., GUNAWAN, G., TALAHATU, M.A., INDRAWATI, RT. & JAMALUDDIN, A. (2013) Resistance analysis of unsymmetrical trimaran model with outboard sidehulls configuration. *Journal of Marine Science and Application* 12 (3), pp. 293–297.